Paper
Int'l J. of Aeronautical & Space Sci. 17(4), 579–592 (2016)
DOI: http://dx.doi.org/10.5139/IJASS.2016.17.4.579

IJASS
International Journal of Aeronautical and Space Sciences

Attitude Control System Design & Verification for CNUSAIL-1 with Solar/Drag Sail

Yeona Yoo*
Satrec Initiative, Daejeon 34054, Republic of Korea

Seungkeun Kim and Jinyoung Suk*****
Chungnam National University, Daejeon 34134, Republic of Korea

Jongrae Kim****
University of Leeds, Leeds LS2 9JT, United Kingdom

Abstract

CNUSAIL-1, to be launched into low-earth orbit, is a cubesat-class satellite equipped with a 2 m × 2 m solar sail. One of CNUSAIL's missions is to deploy its solar sail system, thereby deorbiting the satellite, at the end of the satellite's life. This paper presents the design results of the attitude control system for CNUSAIL-1, which maintains the normal vector of the sail by a 3-axis active attitude stabilization approach. The normal vector can be aligned in two orientations: i) along the anti-nadir direction, which minimizes the aerodynamic drag during the nadir-pointing mode, or ii) along the satellite velocity vector, which maximizes the drag during the deorbiting mode. The attitude control system also includes a B-dot controller for detumbling and an eigen-axis maneuver algorithm. The actuators for the attitude control are magnetic torquers and reaction wheels. The feasibility and performance of the design are verified in high-fidelity nonlinear simulations.

Key words: Attitude control system, Cube satellite, Solar sail, Drag sail

1. Introduction

In recent years, interest in solar and drag sails has been revived. Solar sails use solar radiation pressure (SRP) or aerodynamic drag force for propulsion, which provides continuous acceleration without requiring chemical propellants. Solar sails may realize a novel spacecraft-propelling method for long-duration missions or deep space explorations [1-6]. Meanwhile, drag sails are expected to resolve the debris issue by forcing the satellite to re-enter the atmosphere at the end of its life. Some large-sized sail projects have been suspended because of their high technology costs and failure risks. Instead, small-scaled sail studies have been conducted in low Earth orbit (LEO), as they are significantly less costly to develop and verify.

Small-scale solar sail and drag sail spacecraft include Nanosail-D, Cubesail, Lightsail-1, and Deorbitsail. Nanosail-D, launched by NASA in 2010, was operated in LEO at approximately 600 km altitude. Having experienced orbital decay, its sail was deployed and the satellite re-entered the atmosphere eight months later [7]. Lightsail-1, developed by the Planetary Society and launched in 2015 [8], successfully deployed a 32 m^2 sail, as confirmed by an on-board camera. The orbital decay period of Lightsail-1 was 7 days after sail deployment [9]. Cubesail by Surrey Space Center (SSC) utilized the relative change between the center of mass and the center of solar pressure, and controlled its attitude with magnetic torquers (MTQs) [10]. Cubesail's missions are threefold: to deploy a 25 m^2 solar sail, to operate solar sailing over one year, and to increase the aerodynamic drag force

* Researcher
** Associate Professor, Corresponding author: skim78@cnu.ac.kr
*** Professor
**** Associate Professor

Received: September 14, 2015 Revised: November 23, 2016 Accepted: December 22, 2016

http://ijass.org pISSN: 2093-274x eISSN: 2093-2480

by operating the sail during the deorbiting period. The SSC has also developed DeorbitSail, which is destined for rapid deorbiting from sub-600 km altitudes using a 16 m^2 sail [11].

LEO satellites are easily tumbled by external disturbances. Therefore, the attitude control system is vital for maintaining the communication link to a ground station and requires high battery power. Cube satellite attitude control has been implemented by various control approaches, such as magnetic attitude control [12-15], gravity gradient stabilization [16], and zero-bias momentum using reaction wheels or control moment gyros [17]. Passive magnetic stabilization systems include permanent magnet and hysteresis rods [18-19], spin-control algorithms [20-21], and momentum-biased control combined with MTQs and a momentum wheel.

Attitude control strategies using a solar sail with gimbaled thruster vector control booms, control vanes, and shifting/tilting sail panels have also been studied [22]. However, these strategies cannot be easily applied to cube satellites because of the mass and volume constraints. Nanosail-D uses only a permanent magnet with no active control approaches [23]. Three-axis stabilization is achieved by magnetic torque rods and a translation unit in Cubesail Small Satellite Conference, 2008.

[24], and by a momentum wheel and MTQs in Lightsail-1 [25]. Some solar sail satellites also implement panel translation with magnetic torqueing [26] or reaction wheel/gravity gradient boom stabilization.

The CNUSAIL-1 project, proposed by Chungnam National University in Korea, aims to develop and operate a 4-kg cubic satellite with a small (2 m × 2 m) solar sail. The sail size is determined by the tradeoff between the attitude/orbit dynamics and the control power of the reaction wheel and MTQs. CNUSAIL-1 will be operated in LEO and is targeted for solar sail deployment, stabilized 3-axis attitude control, and deorbiting at the end-of-life.

The main aim of this study is to design an attitude control system for CNUSAIL-1. The design includes 3-axis stabilization using MTQs and a reaction wheel. Two attitude controllers are implemented: i) a B-dot controller for detumbling, and ii) a feedback control algorithm for eigen-axis maneuver under slew rate constraints. The eigen-axis maneuver controller is used during nadir pointing and deorbiting. In most attitude control schemes for cube satellites, a linear quadratic regulator (LQR) or proportional-derivative (PD) controller is considered adequate for small-angle slew maneuvers. However, these schemes cannot guarantee the large-angle slew maneuvers required for attitude pointing, because they are typically implemented by micro-reaction wheel systems in cube-class satellites, which have low slew rate limits. Therefore, torque saturation becomes problematic in large-angle slewing. Especially, the CNUSAIL-1 mission requires large-angle maneuvers such as nadir and velocity-vector pointing for minimizing and maximizing the aerodynamic drag, respectively. During sail deployment, CNUSAIL-1 will experience higher aerodynamic drag than normal cubic satellites. Thus, a feedback control algorithm with slew rate constraints for CNUSAIL-1, which accounts for the realistic saturation limit of the micro-reaction wheel is proposed. The reaction-wheel saturation is relieved by an MTQ manufactured in-house, which plays a momentum dumping role. The proposed scheme is also applicable to future missions of cube satellites requiring large-angle maneuvers by a micro-reaction wheel.

The remainder of this paper is organized as follows. Section 2 introduces the overall and control systems of CNUSAIL-1, and the attitude dynamics. Section 3 presents the controller design for the operational modes (nadir- and velocity-vector pointing). The controller performance is verified by nonlinear simulations in Section 4. Section 5 discusses the performance and limitations of the proposed control scheme, and suggests ideas for future works.

2. Introduction to CNUSAIL-1 system

2.1 System description and mission purpose

The LEO altitude of the CNUSAIL-1 operation was decided from the Cubesat Contest and Developing Program. A relatively high orbital inclination is required. The satellite is built in a 3 U cubesat standard configuration (100 mm× 100 mm× 300 mm), as shown in Fig. 1. Half of this capacity is occupied by the bus system, which includes an attitude determination and control system, an electronic power system, a command and data handling system, and a communication system. The remaining 1.5 U are assigned to the payload (the solar sail deployment system and a camera system). The deployment system is divided into two parts: boom storage and deployment, and membrane storage. The housing volumes of the four quadrant membranes and four booms are 0.5 U and 0.5 U, respectively. Between the payload and bus system, there are two cameras with opposite orientations, which monitor the statuses of sail deployment and health. The satellite base (below the sail membrane) is installed with UHF/VHF antennas, which communicate with a ground station.

The three missions of CNUSAIL-1 are illustrated in Fig. 2. The primary mission is to deploy the solar sail system and operate the satellite in a LEO environment. The secondary

DOI: http://dx.doi.org/10.5139/IJASS.2016.17.4.579

missions are to maneuver the attitude by a spacecraft operation sequence and to deorbit the satellite at the end of its operation life. The purposes of CNUSAIL-1 are to demonstrate the solar sail deployment mechanism, study the orbit and attitude changes, and verify the feasibility of satellite operations with the solar and drag sail. To this end, a 3-axis active attitude stabilization approach is considered, in which the controllers align and maintain the normal vector of the sail in the anti-nadir and velocity vector directions, respectively. The former maneuver (nadir-pointing mode) minimizes the aerodynamic drag and the latter (deorbiting mode) maximizes it.

2.2 Attitude determination and control system

The Attitude Determination & Control System (ADCS) in CNUSAIL-1 directs and maintains the satellite orientation at the desired attitude throughout the solar sail mission. The ADCS controls the attitude such that the normal vector of the solar sail directly opposes the nadir or the velocity vector. ADCS utilizes a 3-axis stabilization system and must operate autonomously without any ground command in its initial mode. Furthermore, the ADCS must maintain its pointing accuracy within 5°, its pointing stability within 0.1°/s, and its pointing knowledge within 3°.

The ADCS comprises an attitude determination system and an attitude control system (enclosed by the dashed and solid rectangles, respectively, in Fig. 3). It includes two types of actuators, four types of sensors, and an attitude determination board. The size of the cubesat-class satellite imposes numerous constraints on the sensors and actuators; size, mass, cost, operational environment, ease of handling, and heritage must all be considered. The sensors and actuators were selected from commercial on-the-shelf (COTS) options, which are conventionally used in small satellite developments. As the attitude sensors, a sun sensor and a magnetometer are selected, and an MEMS gyroscope was chosen as the inertial sensor. The actuators are 3-axis reaction wheels and three MTQs.

The attitude control system operates in three modes: detumbling, nadir-pointing maneuver, and deorbiting maneuver. An ejection from the P-POD triggers antenna deployment and the satellite enters the stabilization mode. When the attitude control system receives the detumbling mode command, it damps the initial angular velocity from its tip-off rate using the MTQs; this action uses only the magnetometer measurements. In the nadir-pointing mode, the aerodynamic drag is parallel to the sail plane, which maximizes the solar radiation force on the satellite while minimizing the drag force. In the deorbiting mode, the aerodynamic force is normal to the sail plane. Hence, the constant aerodynamic force decreases the kinetic energy of the satellite, while solar radiation generates a time-varying force. In both maneuvering modes, the attitude determination system provides the angular rate and attitude estimates using Quaternion ESTimation (QUEST) or extended Kalman filter (EKF) [27].

3. System Dynamic modeling

3.1 Coordinate frames

The body frame fixed at the satellite, the orbital reference

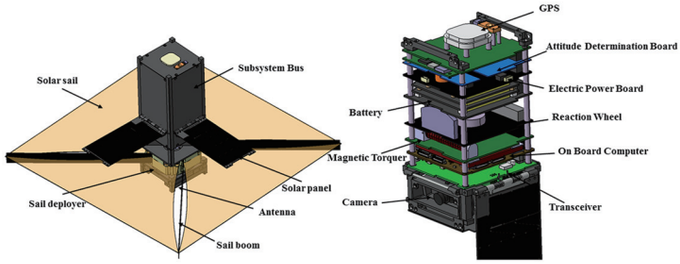

Fig. 1. Schematic of overall configuration of CNUSAIL-1

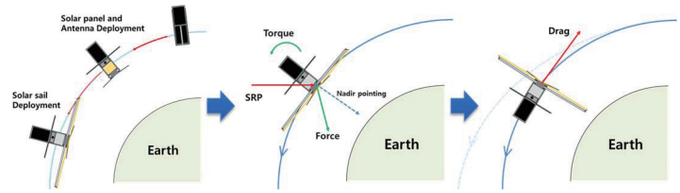

Fig. 2. Operation modes in the CNUSAIL-1 missions

frame, and the Earth-centered inertial frame are denoted by B,R,and E,respectively. The origin of the body frame is the satellite's center of mass. The z axis of the B frame is aligned along the normal vector of the sail; the x and y axes are aligned along the principal axes of inertia following the right-hand rule. The orbital reference frame is centered at the satellite's center of mass and moves along the satellite orbit. The z and y axes of the R frame are directed opposite to the Earth's center and anti-normal to the orbit's direction, respectively, and the x axis is given by the right-hand rule. During nadir-pointing maneuvers, the satellite maintains its desired orientation, in which the body frame coincides with the orbit frame. In the Earth-centered inertial frame, the origin is the center of the Earth, the z axis is perpendicular to the Earth's equatorial plane, the x axis points to the vernal equinox, and the y axis is defined by the right-hand rule. These three coordinate systems are shown in Fig. 4

3.2 Attitude dynamics and kinematics

The rigid body dynamics of the satellite are given by the following Euler equation:

$$\boldsymbol{I}\dot{\boldsymbol{\omega}}_b^I = \mathbf{T}_{dis} + \mathbf{T}_{mag} + \dot{h}_{rw} - \boldsymbol{\omega}_b^I \times (\boldsymbol{I}\boldsymbol{\omega}_b^I + \boldsymbol{h}_{rw}) \tag{1}$$

where $\boldsymbol{I}$ is the moment of inertia matrix, $\boldsymbol{\omega}_b^I$ is the angular velocity of the body frame with respect to the inertial frame, $\mathbf{T}_{dis}$ is the sum of the disturbance torques (namely the aerodynamic, SRP, and gravity-gradient torques), $\mathbf{T}_{mag}$ is the magnetic control torque, and $\boldsymbol{h}_{rw}$ is the angular momentum stored in the reaction wheel.

To avoid kinematic singularities, the attitude between two coordinate systems is expressed as a quaternion, and is governed by the following system of differential equations:

$$\begin{bmatrix}\dot{q}_1\\ \dot{q}_2\\ \dot{q}_3\\ \dot{q}_4\end{bmatrix} = \frac{1}{2}\begin{bmatrix}0 & \omega_{zi} & -\omega_{yi} & \omega_{xi}\\ -\omega_{zi} & 0 & \omega_{xi} & \omega_{yi}\\ \omega_{yi} & -\omega_{xi} & 0 & \omega_{zi}\\ -\omega_{xi} & -\omega_{yi} & -\omega_{zi} & 0\end{bmatrix}\begin{bmatrix}q_1\\ q_2\\ q_3\\ q_4\end{bmatrix} \tag{2}$$

where the body rates, $\omega_{\mathrm{b}}^{\mathrm{i}} = [\omega_{xi}\ \omega_{yi}\ \omega_{zi}]$.

The direction cosine matrix from the ECI to the body frame is expressed as follows:

$$\boldsymbol{R}_{i/b} = \begin{bmatrix}q_1^2 - q_2^2 - q_3^3 + q_4^2 & 2(q_1q_2 + q_3q_4) & 2(q_1q_3 - q_2q_4)\\ 2(q_1q_2 - q_3q_4) & -q_1^2 + q_2^2 - q_3^3 + q_4^2 & 2(q_2q_3 + q_1q_4)\\ 2(q_1q_3 + q_2q_4) & 2(q_2q_3 - q_1q_4) & -q_1^2 - q_2^2 + q_3^3 + q_4^2\end{bmatrix} \tag{3}$$

The direction cosine matrix from the ECI to the orbital reference frame is calculated from the unit vectors of the satellite's position and velocity (denoted r and v, respectively):

$$\boldsymbol{R}_{i/o} = \begin{bmatrix}(v_i \times r_i)^T \times r_i\\ (v_i \times r_i)^T\\ r_i^T\end{bmatrix} \tag{4}$$

3.3 Actuator modeling

3.3.1 Magnetic torquers

MTQs generate torque as the magnetic dipole moment interacts with the geomagnetic field. The MTQs of

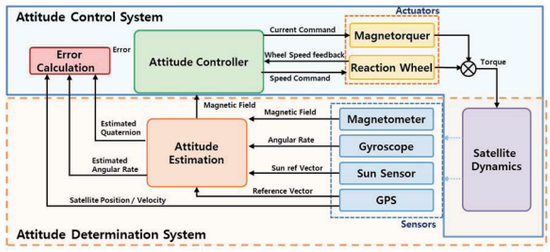

Fig. 3. Block diagram of the Attitude Determination and Control System

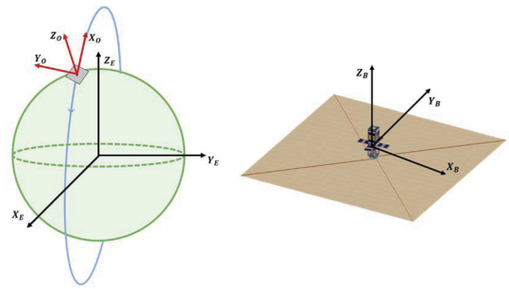

Fig. 4. Illustrations of coordinate frames.

CNUSAIL-1 are designed to satisfy the size constraints of the bus system. Two torquer rods are mounted parallel to the x and y axes in the body frame. The rods are made of copper wire and a nickel–iron magnetic alloy called permalloy. The generated magnetic dipole is 0.02 Am^2 at 0.5 W. An air coil (constructed from an aluminum frame wound with copper wire) is mounted perpendicular to the z axis in the body frame. The air coil provides a dipole moment of 0.01 Am^2 at 0.5 W.

The magnetic torque generates a control torque $\boldsymbol{T}_{mag}$ perpendicular to the Earth's magnetic field. $\boldsymbol{T}_{mag}$ is calculated as

$$\boldsymbol{T}_{mag} = \boldsymbol{M} \times \boldsymbol{B} \tag{5}$$

where $\boldsymbol{B}$ is the geomagnetic field vector and $\boldsymbol{M}$ is the magnetic dipole generated by each rod type is given by [28, 29]:

$$M_{aircoil} = niA \tag{6}$$

$$M_{rod} = \pi r^2 ni \times \left(1 + \frac{\mu_r - 1}{1 + (\mu_r - 1)N_d}\right) \tag{7}$$

In Eqs. (6) and (7), i is the current, n is the number of turns, A is the area of the coil, μ_r is the relative permeability of the core material of the rod, and N_d is the demagnetizing factor. Magnetic coils impose saturation limits on the maximum magnetic moment and coil current. In the present system, the maximum current is 0.1 A, and the maximum command dipole moment is 0.2 Am^2 along the x and y axes and 0.1 Am^2 along the z axis.

During magnetic field measurements by the magnetometer, the MTQ should be deactivated to dissipate its residual dipole moment [30]. Thus, the MTQs are briefly turned off prior to the magnetometer reading.

3.3.2 Reaction wheel

The reaction wheel comprises DC motors and a flywheel, which are assembled on the flywheel axis. The wheel provides an additional moment of inertia and a control torque, enabling high-precision attitude control and fast maneuvers. The cubesat-class 3-axis reaction wheel installed in CNUSAIL-1 was developed and built by Clyde-space Ltd in Scotland. The wheel motors are mounted on a cube-sized PCB board and aligned along the principal axes of the satellite body. Each reaction wheel produces a torque up to 0.196×10^{-3} Nm and stores up to 3.534×10^{-3} Nms of angular momentum.

The governing differential equation of the DC motor inside the reaction wheel, including the back electromotive force (emf) voltage V_b, is

$$V_{in} - V_b = R_M i_M + L\frac{di_M}{dt} \tag{8}$$

where V_{in} is the input voltage to the motor, R_M and L are the resistance and inductance of the motor armature, respectively, and i_M is the motor current. The back emf voltage of the motor is calculated as

$$V_b = K_b \omega_M = K_b(\omega_{rw} - \omega) \tag{9}$$

where K_b is the back emf constant, and ω_M, ω_{rw},and ω are the angular velocities of the wheel relative to the satellite, the wheel motor, and the satellite in the corresponding direction, respectively. The torque output of the motor is calculated by Newton's Law:

$$I_{rw}\ddot{\omega} + K_B\omega_M = T_M \tag{10}$$

where K_B is the viscous friction coefficient. The generated torque T_M is the product of the armature current i_M and the torque coefficient of the motor K_M:

$$T_M = K_M i_M \tag{11}$$

3.4 External disturbance torques

In designing a LEO cube satellite with a solar sail, the disturbance torques by the orbital environment must be considered. The disturbance torques are sourced from the gravity gradient, aerodynamic drag, SRP, and the residual magnetic dipole moment. In the absence of proper control, these disturbances will change the attitude of the satellite or its orbital elements.

3.4.1 Gravity gradient torque

Gravity-gradient torques result from the Earth's gravitational force, which varies with distance and position from the Earth's center. The gravity-gradient torques on the body frame are expressed as [31]

$$T_{gg} = \frac{3\mu}{r_o^3}\boldsymbol{u}_e \times \boldsymbol{I}\boldsymbol{u}_e \tag{12}$$

where μ=3.986·$10^{14}$$m^3/s^2$ is the Earth's gravity constant, r_o is the distance from the Earth's center, $\boldsymbol{u}_e$ is the unit vector in the nadir direction of the fixed body frame, and $\boldsymbol{I}$ is the moment of inertia matrix. The gravity-gradient torques are influenced by the satellite's moment of inertia. Thus, if the moment of inertia increases under solar sail deployment, the gradient torques will also increase.

3.4.2 Aerodynamic drag

LEOs contain residual atmosphere from the Earth, which imposes a drag force on the satellite. The aerodynamic drag acting on the solar sail depends on the atmospheric density, and is given as

$$\mathrm{F}_{\mathrm{aero}} = -\frac{1}{2} C_d \rho |V| \mathbf{V} A \tag{13}$$

where $\vec{\mathrm{F}}_{\mathrm{aero}}$ is the aerodynamic force, C_d is the drag coefficient, $|V|$ is the magnitude of the satellite velocity, A is the projected sail area, and $\vec{V}$ is the velocity vector in the fixed body frame. The atmospheric density ρ is calculated by the NRLMSISE-00 model or an exponential model:

$$\rho = \rho_0 \exp(-\frac{h-h_0}{H}) \tag{14}$$

The aerodynamic torque is generated by the offset between the center of pressure and the center of mass r_{cp}. Specifically, it can be represented

$$\mathrm{T}_{\mathrm{aero}} = \mathrm{r}_{cp} \times \mathrm{F}_{\mathrm{aero}} \tag{15}$$

Because the aerodynamic drag is influenced by the projected sail area and the satellite altitude, the attitude of the satellite with respect to its velocity vector is considered.

3.4.3 Solar radiation pressure

The SRP force is sourced from photons striking the satellite and sail surface in space. The SRP acting on a flat sail surface with the optical properties of the sail material is given by [1]

$$\mathbf{F}_{\mathrm{srp,n}} = -PA\cos\alpha\left((1+rs)\cos\alpha + B_f r(1-s) + \frac{e_f b_f - e_b B_b}{e_f + e_b}(1-r)\right)\mathbf{n} \tag{16}$$

$$\mathbf{F}_{\mathrm{srp,t}} = PA(1-rs)\cos\alpha\sin\alpha\,\mathbf{t} \tag{17}$$

where $\mathbf{F}_{\mathrm{srp}}$ is the SRP, and P=4.563×10^{-6}N/m^2 is the nominal SRP constant at 1 AU from the sun. $\boldsymbol{n}$ and $\boldsymbol{t}$ denote the normal and tangential vectors of the sail, respectively, r is surface reflectivity, and s is the specular reflection coefficient. e_f and e_b are the emission coefficients of the front and back surfaces, respectively, and B_f and B_b are the corresponding non-Lambertian coefficients. The sun angle α is defined as

$$\alpha = \cos^{-1}(\mathbf{S_b} \cdot \mathbf{n}) \tag{18}$$

where S_b=[S_{bx}, S_{by}, S_{bz}]^T is the sun unit vector with respect to the body frame. Furthermore, the sun unit vector will affect either the front or back surface of the solar sail, depending on

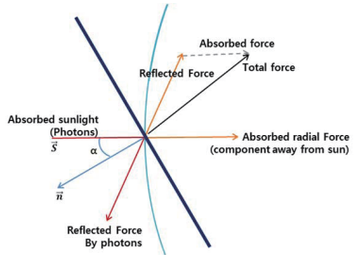

Fig. 5. Solar radiation pressure

the sign of cos(α). Thus, the sail normal vector $\vec{n}$ is redefined as follows:

$$Front: \cos(\alpha) > 0, \text{ then } \vec{n} = [\,0\;\;0\;\;1\,]^{\mathrm{T}} \tag{19}$$

$$back: \cos(\alpha) < 0, \text{ then } \vec{n} = [\,0\;\;0\;\;-1\,]^{\mathrm{T}} \tag{20}$$

$$\mathbf{t} = \left[\frac{\mathrm{S_{bx}}}{\sqrt{S_{xb}^2 + S_{yb}^2}} \quad \frac{\mathrm{S_{by}}}{\sqrt{S_{xb}^2 + S_{yb}^2}} \quad 0\right]^{\mathrm{T}} \tag{21}$$

The SRP torque is calculated similarly to the aerodynamic torque:

$$\mathbf{T}_{srp} = \boldsymbol{r}_{cp} \times \boldsymbol{F}_{srp} \tag{22}$$

3.4.4 Residual magnetic dipole moment

The residual magnetic dipole moment generates a torque by interacting with the geomagnetic field. The resultant torque on the attitude of the satellite is given by

$$\mathbf{T}_{rmd} = \boldsymbol{D} \times \mathbf{B} \tag{23}$$

The residual dipole magnetic moment of the satellite, denoted by $\boldsymbol{D}$, was estimated as $\boldsymbol{D}$=5×10^{-4}Am^2 by PACE CubeSat [32]. The geomagnetic field vector **B** is determined from a model such as IGRF or WMM.

4. Controller design

The attitude control algorithms for CNUSAIL-1 are designed to stabilize the angular rate and achieve the desired attitude. There are three attitude control modes: a detumbling mode, a nadir-pointing maneuver mode, and a deorbiting maneuver mode. The detumbling mode is activated after separation from the P-POD and antenna deployment, and when disturbances increase the angular rate of the satellite. In this mode, the MTQs reduce the angular rate of the satellite until the satellite re-stabilizes. The controller follows the B-dot control law and uses only the magnetometer and MTQ as sensor and actuator, respectively. Once the sail and solar panel are deployed, the operation mode changes to the nadir-pointing mode. The 3-axis stabilization performed by the ACS is applied to the feedback control logic, as proposed in [33], This control points the antenna toward the nadir for communication with a ground station, and for testing the disturbance effect without the aerodynamic drag torque. At the end of the solar sail mission, the operation mode changes to the deorbiting mode. Orbit decay is handled by a feedback control logic similar to the nadir-pointing mode.

DOI: http://dx.doi.org/10.5139/IJASS.2016.17.4.579

4.1 Detumbling mode with B-dot control

When the satellite separates from the P-POD or its angular velocity increases, the ACS enters the detumbling mode as shown in Fig. 6. In this mode, the ACS implements a B-dot controller, which uses the rate of change of magnetic field measured from the magnetometer data. Employing only the magnetometer and MTQ, the controller damps the angular velocity from its initial tip-off rate or increased body rate. The magnetic dipole moment generated along axis i of the B-dot controller is given by

$$M_i = -K\dot{B}_i \quad (i = 1,2,3),\ K > 0, \tag{24}$$

where K is a positive gain and M is the magnetic dipole. $\dot{B}_i$ is the rate of change of the body-fixed geomagnetic field along axis i, estimated by the finite difference method as

$$\dot{B}_i = \frac{B_i(t)-B_i(t-\Delta t)}{\Delta t} \tag{25}$$

with sampling time Δt. $\dot{B}_i$ can also be expressed as the transfer function of a continuous filter [34]

$$\frac{\dot{B}_i}{B_i} = \frac{\omega_c s}{s+\omega_c} = \frac{\omega_c}{1+\omega_c s^{-1}} \tag{26}$$

where ω_c is the cutoff frequency. The resultant control torque by the MTQs, which is generated perpendicular to the Earth's magnetic field, is then given by

$$\boldsymbol{T}_{mag} = \boldsymbol{M} \times \boldsymbol{B} \tag{27}$$

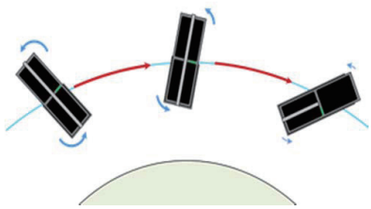

Fig. 6. Detumbling mode

4.2 Nadir pointing/deorbiting based on eigen-axis maneuvers under slew rate constraints

In LEO environments, solar sail missions require that the aerodynamic drag be minimized. The radio signals from the antenna cannot penetrate the sail membranes; therefore, satellite–ground communication depends on the satellite attitude. For this reason, the satellite attitude is aligned with the orbit reference frame. In this alignment, the sail plane is perpendicular to the orbital plane and the aerodynamic drag is minimized; moreover, the antenna located at the base of the satellite points toward the nadir, where it can communicate with the ground station. Thus, in the nadir-pointing maneuver mode, the satellite maintains the nadir pointing orientation within 5° normal to the solar sail, which minimizes the aerodynamic drag. In the deorbiting maneuver mode, the satellite rotates 90° from the nadir pointing attitude to align with the velocity vector normal to the solar sail. This orientation maximizes the aerodynamic drag. The ACS will use the 3-axis reaction wheel for maneuvering and the magnetic torque for momentum dumping.

Generally, satellite maneuvers adopt a linear controller such as PD or LQR. However, these controllers are unsuitable for large-angle maneuvers because they tend to saturate the reaction wheel momentum or torque. Thus, in this study, the nadir pointing and deorbiting maneuvers are implemented by a feedback control logic for eigen-axis maneuver under slew rate constraints [34].

Considering the maximum slew rate about the eigen-axis, the control torque is given as [33].

$$\boldsymbol{u} = -\boldsymbol{K}sat(\boldsymbol{P}\boldsymbol{q}_e) - \boldsymbol{C}\boldsymbol{\omega}_e + \boldsymbol{\omega} \times \boldsymbol{I}\boldsymbol{\omega} \tag{28}$$

where

$$\boldsymbol{K} = \mathrm{diag}(\mathrm{k}_1, k_2, k_3)\boldsymbol{I} \tag{29}$$

$$\boldsymbol{P} = \mathrm{diag}(p_1, p_2, p_3) \tag{30}$$

$$\boldsymbol{C} = c\boldsymbol{I} \tag{31}$$

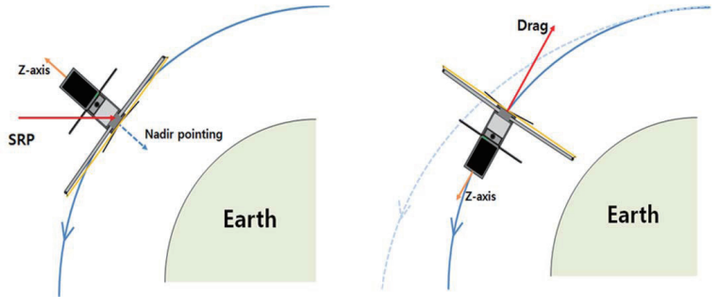

Fig. 7. Nadir pointing/ Deorbiting maneuver mode

The last term in Eq.(28) is a kind of nonlinear control to cancel ω×Iω in Eq.(1) to linearize the closed-loop dynamics. The saturation function is defined as:

$$\mathrm{sat}(\mathrm{Pq_e})_i = \begin{cases} 1 & , \quad Pq_{e,i} > 1 \\ Pq_{e,i} & , -1 \le Pq_{e,i} \le 1 \\ -1 & , \quad Pq_{e,i} < -1 \end{cases} \tag{32}$$

The positive scalar gain k_i, p_i can defined as:

$$\mathrm{k_i} = \mathrm{c} * \frac{\mathrm{q_{e,o}}}{|\mathrm{q_{e,o}}|} * \dot{\theta}_{max} \tag{33}$$

$$\boldsymbol{KP} = k\boldsymbol{I} \tag{34}$$

where $\dot{\theta}_{max}$ is the maximum slew rate. Following [33], it is assumed that $q_{e,0}$≠0 and $\omega(0)$=0. k and c are then chosen as

$$k = 2\omega_{\mathrm{n}}^2 \tag{35}$$

$$c = 2\zeta\omega_n \tag{36}$$

where k and c are the desired damping ratio and the natural frequency, respectively. The quaternion error, denoted by $\mathrm{q_e}=[\mathrm{q_{e1}}\ \mathrm{q_{e2}}\ \mathrm{q_{e3}}]^T$ is defined

$$\begin{bmatrix} q_{e1} \\ q_{e2} \\ q_{e3} \\ q_{e4} \end{bmatrix} = \frac{1}{2} \begin{bmatrix} q_{c4} & q_{c3} & -d_{c2} & -q_{c1} \\ -q_{c3} & q_{c4} & q_{c1} & -q_{c2} \\ q_{c2} & -q_{c1} & q_{c4} & -q_{c3} \\ q_{c1} & q_{c2} & q_{c3} & q_{c4} \end{bmatrix} \begin{bmatrix} q_1 \\ q_2 \\ q_3 \\ q_4 \end{bmatrix} \tag{37}$$

where q_{ci} are the command quaternions and q_i are the satellite attitude quaternions. The error in the angular velocity, denoted $\boldsymbol{\omega}_e=[\omega_{\mathrm{e1}}\ \omega_{e2}\ \omega_{\mathrm{e3}}]^T$ is defined as:

$$\boldsymbol{\omega}_e = \boldsymbol{\omega} - \boldsymbol{R}_{o/b}[0 \ \ -\omega_0 \ \ 0]^T \tag{38}$$

4.3 Unloading of the reaction wheel momentum by the MTQ

The momentum of the reaction wheel increases under constant external disturbance. If the momentum exceeds the storage limits, the reaction wheel becomes saturated and unable to produce the control torque. Hence, the excess momentum should be unloaded by MTQs. The momentum unloading logic is defined as [35]

$$\mathbf{m} = -\frac{\mathrm{k_{rw}}}{B^2}(\mathbf{B} \times \Delta\mathbf{h}) \tag{39}$$

where k_{rw} is the unloading control gain, and $\Delta\boldsymbol{h}$ is the error between the current and desired wheel momentum vectors. However, removing the stored momentum by a magnetic torque compromises the power of the satellite. Thus, the unloading logic is operated when the momentum exceeds a specified limit.

5. Numerical simulation

5.1 Simulation Conditions

The aerodynamic drag, SRP, gravity gradient disturbances, and the effect of the residual magnetic dipole moment were evaluated in numerical simulations. The orbit parameters of CNUSAIL-1 are listed in Table 1. The orbital propagation is subjected to a J2 perturbation. The geomagnetic field model is implemented in International Geomagnetic Reference Field 2011 (IGRF-11). The sun location is calculated from the Julian date.

The moment of inertia is represented in the body frame. The optical properties are those of metalized kapton sheet, from which the solar sail is constructed. The satellite and optical properties before and after the sail deployment are listed in Tables 2 and 3Table 3, respectively.

Table 4 and Table 5 list the specifications of the reaction wheel and the MTQs, respectively. The reaction wheel unloading logic is activated when the angular velocity of the reaction wheel reaches 3000 rpm (corresponding to an angular momentum of 1.35×10^{-3} Nms).

5.2 Detumbling mode

The detumbling mode activates under two scenarios: the

Table 1. Orbital parameters of CNUSAIL-1

Element	Description
Semi-major axis a	6963.1 km
Inclination	98°
Eccentricity	0.01939
LTDN	10:30
Orbit Period	84.50 min

Table 2. Satellite properties

Element		Description
mass		4 kg
Sail Area		4 m^2
Moment of Inertia	Pre-deployed	(0.0506, 0.0506, 0.010)
(I_x, I_y, I_z) [kg m^2]	Post-deployed	(0.3104, 0.3121, 0.5757)

Table 3. Optical properties of the solar sail [37]

Element	Description
Front emission coefficient B_f	0.79
Back emission coefficient B_B	0.55
Front non-Lambertian coefficient e_f	0.05
Back non-Lambertian coefficient e_b	0.55
Reflectivity r	0.88
Specular reflection coefficient s	0.94

DOI: http://dx.doi.org/10.5139/IJASS.2016.17.4.579

initial tip-off after the satellite separates from the P-POD, and when the angular rate of the satellite increases above 1°/s. The solar sail is deployed by a spiral spring torque, increasing the moment of inertia and reducing the angular rate of the satellite to almost zero [36]. When simulating the post-deployment detumbling mode, the initial angular rate is assumed lower than the pre-deployment rate; that is,

Pre-deployment: ω=[6 -7 3]^{T} °/s

Post-deployment: ω=[2 -7 1]^{T} °/s

Table 4. Specifications of reaction wheel

Element	Description
Manufacturer	Clyde-space Ltd
Mass	0.275 kg
Inertia	4.5e-6 kg m^2
Maximum torque	1.9 × 10^{-3}Nm
Maximum Momentum	3.4 × 10^{-3}Nms
Maximum Angular rate	7000 RPM

Table 5. Specifications of magnetic torquer

Element		Description
Torquer rod	Length (x, y)	60 mm
	Radius	4 mm
	Dipole moment	0.2 Am^2
Air Coil	Area (z)	65mm x 75mm
	Dipole moment	0.1 Am2

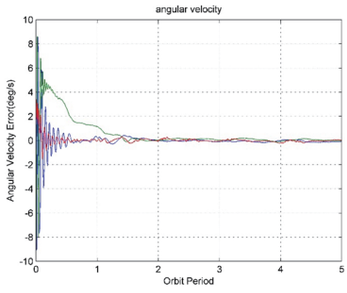

Fig. 8. B-dot controller verification (pre-deployment)

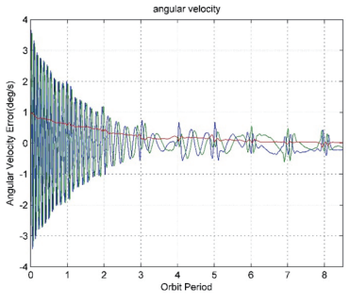

Fig. 9. B-dot controller verification (post-deployment)

The detumbling gain factor K is set to 30000 and 50000 in the pre- and post-deployment cases, respectively. The sampling period of the magnetometer and MTQ is 2 s. The simulated angular rates during pre- and post-deployment are plotted in Figs. 8 and 9, respectively. In the pre-deployment case, the angular rate reduces below the desired level for the nadir-pointing maneuver after approximately three orbits. In the post-deployment case, the reaction wheels reduce the angular rates to below 1°/s. However, the satellite sways periodically under the larger aerodynamic drag torque than in the pre-deployment case.

5.3 Nadir-pointing and deorbiting maneuver modes under slew rate constraints

5.3.1 Nadir-pointing maneuver

The initial error quaternion in the large-angle maneuver simulation is set to

$q_{e,0}$=[0.6460 0.2876 -0.6460 0.2876]^{T}

where the initial error in the angular velocity is zero. The unloading logic will be activated when the angular rate of the reaction wheel exceeds 3000 rpm. The maximum slew rate is set to 0.3°/s, and the initial eigen-angle is 146.5°. Ideally, an optimal attitude control would require 8.13 min to complete the maneuver.

Fig. 10–13 and Figs. 14–18 plot the simulation results in the pre- and post-deployment cases, respectively. The nadir-pointing maneuver is completed under the slew rate constraints in both

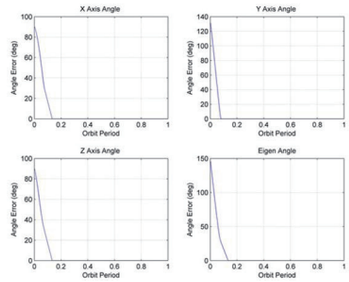

Fig. 10. Attitude error (pre-deployment)

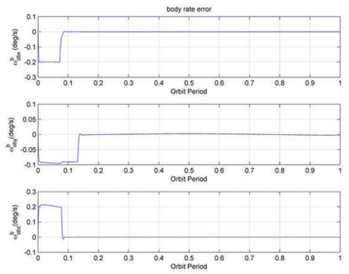

Fig. 11. Body rate error (pre-deployment)

cases. In the post-deployment case, momentum unloading is also activated. As shown in Fig. 17, the reaction speeds along the x and z axes are below 3000 rpm, so the magnetic dipole moment command is not issued around the y axis.

5.3.2 Comparisons between PD control logic and eigen-axis maneuvering under slew rate constraints

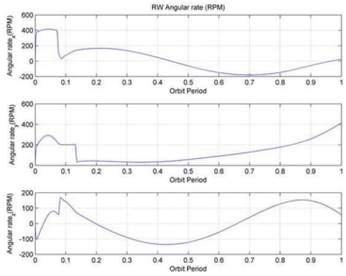

Fig. 12. Reaction wheel Angular rate (pre-deployment)

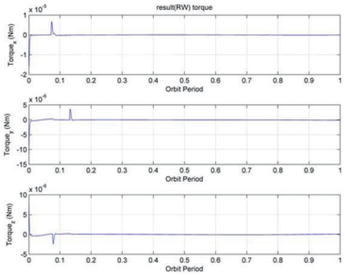

Fig. 13. Command torque (pre-deployment)

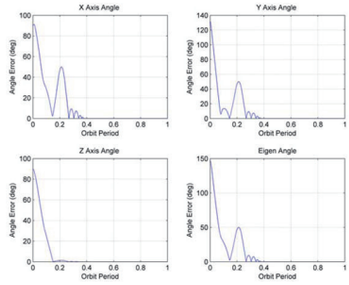

Fig. 14. Attitude error (post-deployment)

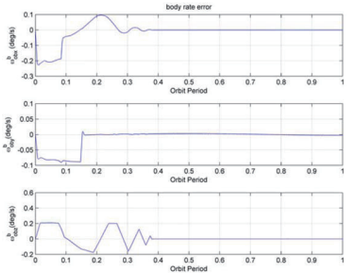

Fig. 15. Body rate error (post-deployment)

This subsection compares the eigen-axis maneuvering algorithm with the PD control logic which is given by

$$u = -Kq_e - C\omega_e \tag{40}$$

Fig. 20 plot the attitude errors during a large-angle maneuver controlled by the PD logic and the eigen-axis

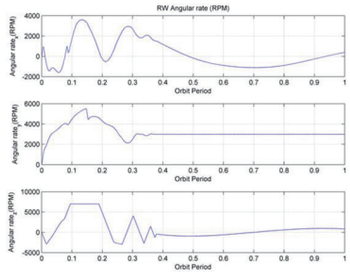

Fig. 16. Reaction wheel Angular rate (post-deployment)

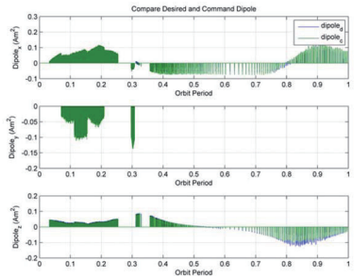

Fig. 17. Magnetic dipole command for momentum unloading (post-deployment)

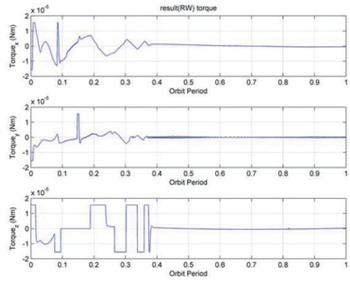

Fig. 18. Command torque (post-deployment)

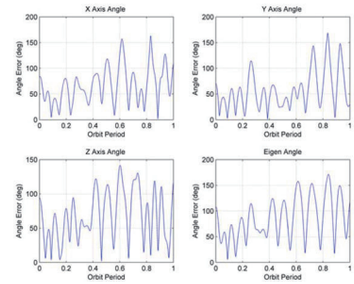

Fig. 19. Errors in large-angle maneuver controlled by PD control logic

DOI: http://dx.doi.org/10.5139/IJASS.2016.17.4.579

algorithm (with eigen-angle = 108°), respectively, in the post-deployment case. Unlike the PD control logic, the eigen-axis maneuvering algorithm achieved the desired nadir pointing.

5.3.3 Deorbiting maneuver

The deorbiting maneuver signifies the end of the satellite operation in the solar sail mission. During this operation, the satellite maintains the nadir-pointing position. In the simulation, the initial error quaternion is set to $q_{e,0}$=[-0.0000 0.7071 -0.0000 0.7071]^{T}
where the initial error angular velocities are set to zero.

This case, however, compromises the $q_{e,0}\neq 0$ condition. The control gain matrix P cannot exist for a zero-valued error quaternion. Hence, when $q_{e,0}$<0.1, the error quaternions are redefined as

$q_{e,0}$=[-0.1 0.7071 -0.1 0.7071]^{T}

Accordingly, the eigen-angle error in the gain calculation increases by approximately 1.15°.

Fig. 21 –25 plot the angular rate error, attitude angle error, wheel angular rate, and the control torque, respectively. The satellite is initially aligned with the orbital reference frame. The first phase completes the deorbiting maneuver. In the second phase, which is in perigee with the maximum aerodynamic drag torque, the reaction wheels are saturated and the satellite fails to achieve the desired attitude. The error in the second phase exceeds the initial error and the controller shows poor performance, because the gain was calculated using the initial error. The angular errors are 20° above the initial angular error and the control gain is updated by the current error quaternion through Eqs. (29)–(34). The simulation results after the gain recalculation are presented in Figs. 26–30. The deorbiting maneuver is now partially achieved under the slew rate constraints and the satellite nearly maintains the attitude that maximizes the aerodynamic drag. The satellite periodically tumbles and the reaction wheel saturates under the aerodynamic drag torque.

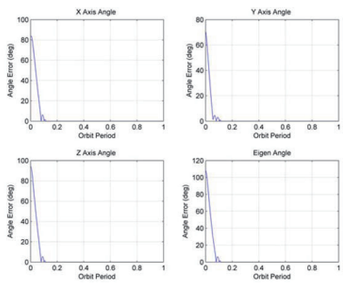

Fig. 20. Errors in large-angle maneuver controlled by eigen-axis maneuver logic

5.3.4 Life time analysis

The forces imposed on the sail plane change the altitude of the cube satellite. Fig. 31 plots the altitude decrease at the semi-major axis under random angular rate rotations, the

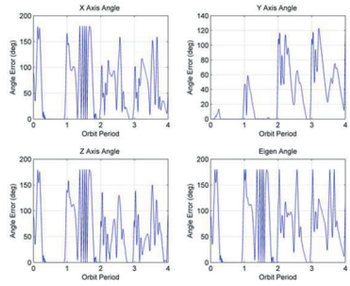

Fig. 21. Attitude error (deorbiting, initial gain maintain)

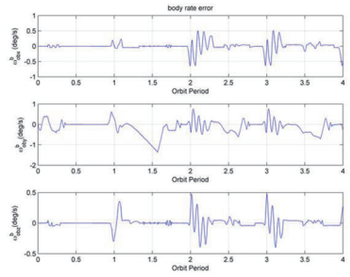

Fig. 22. Body rate error (deorbiting, initial gain maintenance)

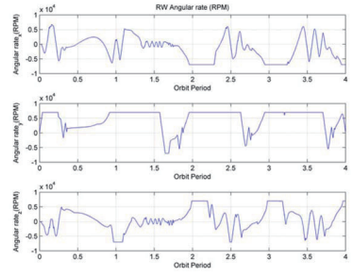

Fig. 23. Reaction wheel angular rate (deorbiting, initial gain maintenance)

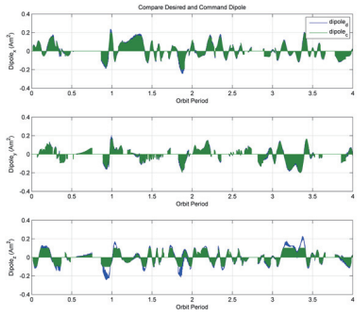

Fig. 24. Magnetic dipole command for momentum unloading (deorbiting, initial gain maintenance)

nadir-pointing maneuver, and the deorbiting maneuver. In the case of random angular rate rotations, the satellite orbit decays over 40 days. The orbital decay rate is increased in the deorbiting mode, occurring after approximately 24 days. Fig. 32 compares the lifetime of CNUSAIL-1 with those of existing cube satellites. The lifetime analysis of CNUSAIL-1 compares reasonably with the real data of Lightsail-1 and Nanosail-D.

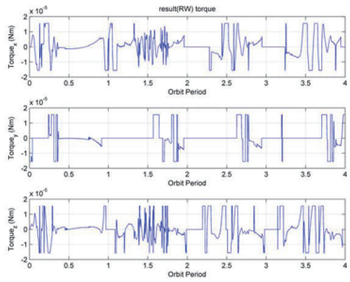

Fig. 25. Command torque (deorbiting, initial gain maintenance)

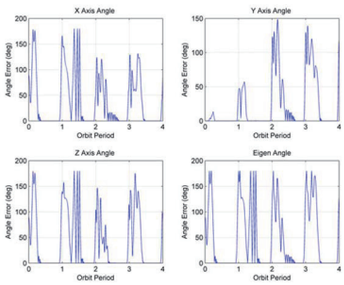

Fig. 26. Attitude error (deorbiting, gain recalculation)

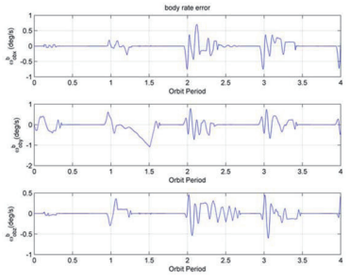

Fig. 27. Body rate error (deorbiting, gain recalculation)

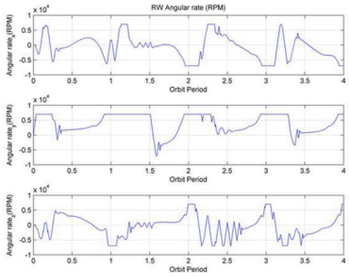

Fig. 28. Reaction wheel angular rate (deorbiting, gain recalculation)

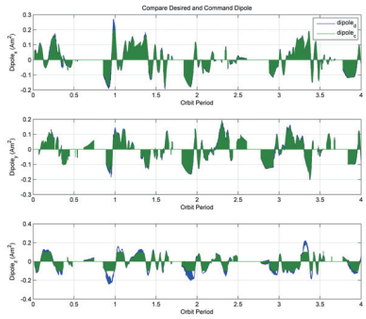

Fig. 29. Magnetic dipole command for momentum unloading (deorbiting, gain recalculation)

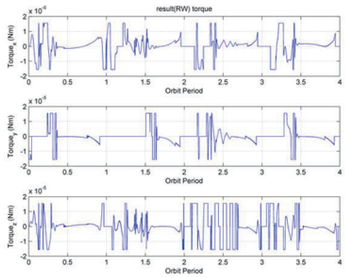

Fig. 30. Command torque (deorbiting, gain recalculation)

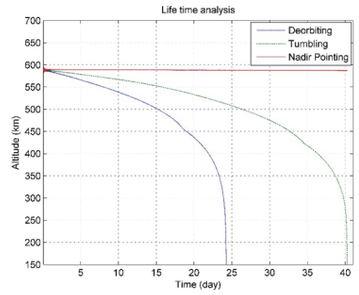

Fig. 31. Simulated lifetime analysis of CNUSAIL-1

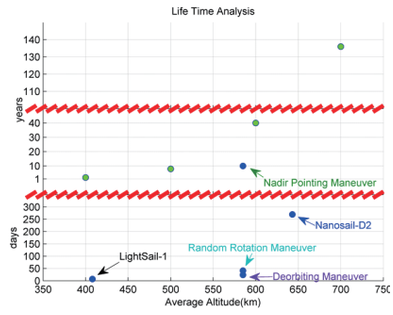

Fig. 32. Lifetimes of CNUSAIL-1 in random rotation, deorbiting, and nadir-pointing maneuvers. Lifetimes of real cubesats (Nanosail-D2 and Lightsail-1) are shown for comparison. Green dots are the estimated lifetimes of the 3U-scaled cube satellites in circular orbits.

DOI: http://dx.doi.org/10.5139/IJASS.2016.17.4.579

In the nadir-pointing maneuver, the satellite will operate for approximately 10 years, similar to cube satellites without a solar sail. However, satellites maintaining the deorbiting mode or random rotation will undergo faster orbital decay than standard cube satellites.

6. Conclusions

This paper presented and analyzed the attitude control system of CNUSAIL-1. The missions of CNUSAIL-1 are to demonstrate the solar sail mechanism and to study the effects of installing the sail, especially on satellite orbit and attitude. The satellite and the nadir-pointing and deorbiting maneuvers were stabilized by three attitude control modes and two control logic modes. Simulations verified that the proposed attitude control system achieves the desired attitude in both pre- and post-deployment modes of the sail. As required, the 3-axis stabilization controller maintained the nadir pointing accuracy within 5°. The pointing tolerance of the deorbiting maneuver was partially satisfied and the satellite re-entered the atmosphere within 40 days. These high-fidelity simulation-based analyses of attitude control for sail operation in LEO is due to be verified by a real operation after orbit injection by Falcon-9 in the first quarter of 2016.

Acknowledgement

This research was supported by Space Core Technology Development Program and Cubesat Contest and Developing Program through the National Research Foundation of Korea (NRF) and the Korea Aerospace Research Institute (KARI) funded by the Korea government (Ministry of Science, ICT and Future Planning)(No. NRF-2014M1A3A3A02034925, and NRF-2013M1A3A4A01075962).

References

[1] McInnes, C. R., *Solar Sailing: Technology, Dynamics and Mission Applications*, Springer Science & Business Media, 2013.

[2] Jenkins, C. M., "Progress in Astronautics and Aeronautics: Gossamer Spacecraft: Membrane and Inflatable Structures Technology for Space Applications", AIAA, Vol. 191, 2001.

[3] Gershman, R. and Seybold, C., "Propulsion Trades for Space Science Missions", *Acta Astronautica*, Vol. 45, No. 4, 1999, pp. 541-548.

[4] Reichhardt, T., "Space Technology: Setting Sail for History", *Nature*, Vol. 433, No. 7027, 2005, pp. 678-679.

[5] Garner, C., Diedrich, B., and Leipold, M. "A Summary of Solar Sail Technology Developments and Proposed Demonstration Missions", *35th AIAA Joint Propulsion Conference*, 1999.

[6] Jenkins, C.H., Gough, A.R., Pappa, R.S., Carroll, J., Blandino, J.R., Miles, J.J. and Rakoczy, J., "Design Considerations for An Integrated Solar Sail Diagnostics System", *AIAA Paper*, Vol. 1510, 2004.

[7] Johnson, L., Whorton, M., Heaton, A., Pinson, R., Laue, G. and Adams, C., "NanoSail-D: A Solar Sail Demonstration Mission," *Acta Astronautica*, Vol. 68, No. 5, 2011, pp. 571-575.

[8] Biddy, C., and Svitek, T., "LightSail-1 Solar Sail Design and Qualification", *Proceedings of the 41st Aerospace Mechanisms Symposium*, 2012.

[9] Davis, J., "LightSail Test Mission Ends with Fiery Reentry," http://www.planetary.org/blogs/jason-davis/, accessed on 18 June 2015.

[10] Staehle, R.L., Blaney, D., Hemmati, H., Lo, M., Mouroulis, P., Pingree, P., Wilson, T., Puig-Suari, J., Williams, A., Betts, B. and Friedman, L., "Interplanetary CubeSats: opening the solar system to a broad community at lower cost," *CubeSat Workshop*, Logan, UT, USA, 2011, pp. 6-7.

[11] Surrey Space Centre, "Deorbitsail mission," http://www.surrey.ac.uk/ssc/research/space_vehicle_control/deorbitsail/mission/index.htm, accessed on 20 July 2015.

[12] Lorentzen, T., "Attitude control and determination system for DTUsat1," CubeSat Project, Department of Automation, Orsted DTU, 2002.

[13] Reichel, F., Bangert, P., Busch, S., Ravandoor, K. and Schilling, K., "The attitude determination and control system of the picosatellite uwe-3," *IFAC Proceedings*, Vol. 46, No. 19, 2013, pp.271-276.

[14] Bråthen, G., "Design of attitude control system of a double cubesat," Master's Thesis, NTNU, 2013.

[15] Jensen, K.F. and Vinther, K., "Attitude determination and control system for AAUSAT3," Master's Thesis, Aalborg University, 2010.

[16] Rawashdeh, S.A., "Passive attitude stabilization for small satellites," Master's Thesis, University of Kentucky, 2010.

[17] Lee, S.M., Seo, H-H, and Rhee, S-W., "Design and Practical Results of Four-CMG Cluster for Small Satellites," *International Journal of Aeronautical and Space Sciences*, Vol. 8, No. 1, 2007, pp. 105-114.

[18] Santoni, F., and Zelli, M., "Passive magnetic attitude stabilization of the UNISAT-4 microsatellite," *Acta Astronautica*, Vol. 65, No. 5, 2009, pp. 792-803.

[19] Barabash, S., et al., "The nanosatellite Munin, a simple tool for auroral research," *Advances in Space Research*, Vol. 31, No. 2, 2003, pp. 313-318.

[20] Ridge, C. and Healy, C., "The Magnetic Attitude Control System for the Parkinson Satellite (PSAT) A US Naval Academy Designed CubeSat", *AIAA Guidance, Navigation, and Control Conference*, Chicago, Illinois, 2009.

[21] Vega, K., Auslander, D. and Pankow, D., "Design and modeling of an active attitude control system for CubeSat class satellites," *AIAA Modeling and Simulation Technologies Conference*, 2009.

[22] Wie, B., "Solar sail attitude control and dynamics, Part 2," *Journal of Guidance, Control, and Dynamics*, Vol. 27, No. 4, 2004, pp. 536-544.

[23] Whorton, M., Heaton, A., Pinson, R., Laue, G. and Adams, C., "Nanosail-D: the first flight demonstration of solar sails for nanosatellites," *Small Satellite Conference*, 2008.

[24] Lappas, V., Adeli, N., Visagie, L., Fernandez, J., Theodorou, T., Steyn, W. and Perren, M., "CubeSail: A low cost CubeSat based solar sail demonstration mission," *Advances in Space Research*, Vol. 48, No. 11, pp.1890-1901.

[25] Nehrenz, M.T., "Initial design and simulation of the attitude determination and control system for LightSail-1," BS Thesis, California Polytechnic State University - San Luis Obispo, 2010.

[26] Steyn, W.H. and Lappas, V., "Cubesat solar sail 3-axis stabilization using panel translation and magnetic torqueing," *Aerospace Science and Technology*, Vol. 15, No. 6, 2011, pp.476-485.

[27] Kim, G., Kim, S., Suk, J. and Kim, J.R., "Attitude Determination Algorithm Design and Performance Analysis for CNUSAIL-1 Cube Satellite," *Journal of the Korean Society for Aeronautical & Space Sciences*, Vol. 43, No. 7, 2015, pp.609-618.

[28] Jayaram, S., "Design of template to fabricate magnetic torquer coils for nano and picosatellite missions," *Journal of Engineering, Design and Technolo*gy, Vol. 8, No. 2, 2010, pp. 158-167.

[29] Mehrjardi, M.F. and Mehran M., "Design and manufacturing of a research magnetic torquer rod," *Fourth International Conference on Experimental Mechanics*, 2009.

[30] De Ruiter, A.H., Damaren, C. and Forbes, J.R., *Spacecraft Dynamics and Control: An Introduction*, John Wiley & Sons., 2012.

[31] Wertz, J.R., *Spacecraft attitude determination and control*, Vol. 73, Springer Science & Business Media, 2012.

[32] Springmann, J.C., Cutler, J.W. and Bahcivan, H., "Magnetic sensor calibration and residual dipole characterization for application to nanosatellites," *AIAA/ AAS Astrodynamics Specialist Conference*, Toronto, Ontario Canada, 2010.

[33] Wie, B. and Lu, J., "Feedback control logic for spacecraft eigenaxis rotations under slew rate and control constraints," *Journal of Guidance, Control, and Dynamics*, Vol. 18, No. 6, 1995, pp. 1372-1379.

[34] Jensen, K.F. and Kasper. V., "Attitude Determination and control system for AAUSAT3," Master's Thesis, Aalborg University, 2010.

[35] Sidi, M.J., *Spacecraft dynamics and control: a practical engineering approach*, Vol. 7. Cambridge university press, 1997.

[36] Adeli, S.N. and Lappas, V.J., "Deployment system for the CubeSail nano-solar sail mission," *24th ASU/AIAA Annual Conference on Small Satellites*, Logan, Utah, 2010.

[37] Wright, J.L., *Space sailing*, Taylor & Francis, 1992.

DOI: http://dx.doi.org/10.5139/IJASS.2016.17.4.579